Earth and Planetary Science Letters 443 (2016) 139–152

Contents lists available at ScienceDirect

Earth and Planetary Science Letters

www.elsevier.com/locate/epsl

Two pulses of oceanic environmental disturbance during the Permian–Triassic boundary crisis

Jun Shen [a,*], Qinglai Feng [a], Thomas J. Algeo [a,b,c,*], Chao Li [b], Noah J. Planavsky [d], Lian Zhou [a], Mingliang Zhang [a]

[a] State Key Laboratory of Geological Processes and Mineral Resources, China University of Geosciences, Wuhan, Hubei, 430074, PR China
[b] State Key Laboratory of Biogeology and Environmental Geology, China University of Geosciences, Wuhan, Hubei, 430074, PR China
[c] Department of Geology, University of Cincinnati, Cincinnati, OH 45221-0013, USA
[d] Department Geology and Geophysics, Yale University, New Haven, CT 06520-8109, USA

ARTICLE INFO

Article history:
Received 13 December 2015
Received in revised form 9 March 2016
Accepted 14 March 2016
Available online 30 March 2016
Editor: M. Frank

Keywords:
Permian–Triassic
Fe speciation
pyrite
sulfur isotopes
framboids
paleoceanography

ABSTRACT

Pyrite morphology, iron speciation, and pyrite sulfur isotope data from the Xiakou section (Hubei Province, South China) were integrated to explore oceanic environmental variations through the Permian–Triassic transition and their possible relations to the largest mass extinction in Earth history. High ratios of highly-reactive iron to total iron ($Fe_{HR}/Fe_T > 0.6$) and pyrite iron to highly-reactive iron ($Fe_{Py}/Fe_{HR} > 0.7$) together with a high abundance of small (mean diameter <5 μm) framboidal pyrite show that euxinic conditions existed in the late Permian (pre-extinction interval). High ratios of Fe_{HR}/Fe_T (mostly >0.6) along with lower values of Fe_{Py}/Fe_{HR} (<0.7) and more variable framboid content among samples indicate anoxic but dominantly ferruginous conditions punctuated by episodic euxinic events in the latest Permian to earliest Triassic (post-extinction interval). The largest fluctuations of these redox proxies are observed in the ~1.0 m of strata directly overlying the first (latest Permian) extinction horizon, indicating unsettled marine environmental conditions marked by frequent perturbations during the ~60-kyr interval immediately following the mass extinction. The two largest redox events at Xiakou coincided with deposition of volcanic ash layers that have been correlated with Beds 25 and 28 of the Meishan D section, each of which was associated with an extinction pulse (the first and second extinction horizons of latest Permian and earliest Triassic age, respectively). Thus, our observations document two pulses of oceanic environmental change during the Permian–Triassic transition, each associated with a faunal crisis and possibly triggered by contemporaneous volcanic activity.

1. Introduction

The Permian–Triassic transition is a key interval in Earth history owing to long-lasting, concurrent, and interrelated changes in the biosphere and environment (Erwin et al., 2002). The end of the Permian witnessed the largest mass extinction in Earth history, with ~90% of marine invertebrate species and ~70% of terrestrial vertebrate species killed off within ~60 kyr (Erwin et al., 2002; Shen SZ et al., 2011). Following the latest Permian mass extinction (LPME), the initial ~5 Myr of the Early Triassic were marked by global climatic and environmental upheavals, as recorded by large carbon and sulfur isotope excursions (e.g., Song et al., 2014), intensified weathering (Algeo and Twitchett, 2010), widespread ocean anoxia (Wignall and Twitchett, 1996; Isozaki, 1997; Grice et al., 2005), lethally hot temperatures (Sun et al., 2012), and repeated biocrises that delayed full recovery of marine ecosystems (Chen and Benton, 2012). Eruption of the Siberian Traps large igneous province (LIP) is widely regarded as the trigger for the Permian–Triassic boundary (PTB) crisis (Reichow et al., 2009; Bond and Wignall, 2014), although the processes linking this eruption to the LPME remain a subject of intense research. Regional volcanism around the PTB also has been proposed as a source of volcanic ash in the South China area (Yin et al., 1992).

The pattern of extinction and environmental perturbation during the Permian–Triassic transition has slowly come into focus through high-resolution bio- and chemostratigraphic studies. Statistical analysis of 333 marine invertebrate species belonging to 162 genera in the PTB global stratotype section and point (GSSP)

* Corresponding authors.
E-mail addresses: shenjun_2009@163.com (J. Shen), Thomas.Algeo@uc.edu (T.J. Algeo).

http://dx.doi.org/10.1016/j.epsl.2016.03.030
0012-821X/

at Meishan D in Zhejiang Province, China, led Jin et al. (2000) to identify a large, rapid extinction event coincident with Bed 25 and a smaller secondary event coincident with Bed 28. These two phases of the mass extinction were examined in greater detail through analysis of the bioranges of 537 species representing 17 marine groups by Song HJ et al. (2013) and analysis of biomarkers for photic-zone euxinia and nitrogen fixation recording concurrent changes in marine microbial communities by Xie et al. (2005, 2007). Patterns of biotic and environmental changes at the PTB and their possible underlying causes were summarized by Yin et al. (2012). Many climatic and oceanographic proxies exhibit major shifts around the PTB, but apart from carbonate $\delta^{13}C$ records (Xie et al., 2007), none of these proxies has been shown to exhibit two distinct pulses coinciding with the two-phased biotic crisis.

In this contribution, we undertake a high-resolution (centimeter-scale) stratigraphic analysis of iron speciation, pyrite morphology, and pyrite sulfur isotopes in the deep cratonic shelf section at Xiakou, Hubei Province, China. Although the study section has been the subject of numerous earlier biostratigraphic, sedimentologic, and geochemical investigations (Shen et al., 2015, and references therein), the present study is the first to generate iron speciation, pyrite morphology, and pyrite sulfur isotope data for Xiakou. Our primary goals are to determine (1) the timing of the LPME relative to penecontemporaneous marine environmental changes, and (2) whether high-resolution deep-water marine sections can provide evidence of two distinct pulses of environmental change during the Permian–Triassic transition that are difficult to resolve in shallow-marine sections owing to the presence of a lowstand stratigraphic hiatus (e.g., Yin et al., 2014).

2. Geological setting and stratigraphy

South China was a small craton located in the eastern part of the Paleo-Tethys near the equator during the Permian–Triassic transition (Fig. 1A). Alluvial facies and shallow-marine siliciclastic sediments derived from the Cathaysia and Kangdian oldlands accumulated on its northeastern and southern margins, respectively (Fig. 1B; note: all cited compass directions refer to end-Permian paleogeography, prior to a ~90° clockwise rotation of the South China Craton during the Mesozoic). The central part of the craton was occupied by the shallow carbonate Yangtze Platform. A deeper carbonate ramp descended from the Yangtze Platform toward the Qinling Sea in the west. Black siliceous and carbonate mudstones and argillaceous limestones were the main deposits on this ramp, which was a site of continent-margin upwelling (Fig. 1B). The deepwater Nanpanjiang Basin to the southeast of the Yangtze Platform accumulated similar facies containing abundant radiolarians, brachiopods, bivalves, and sponges (Feng et al., 2007). Sedimentation in these two basinal settings was continuous through the Permian–Triassic transition, yielding an unbroken record of paleoceanic conditions, whereas contemporaneous shallow-water settings are commonly condensed or interrupted by hiatuses (Yin et al., 2014).

The Xiakou section (GPS: N31°06.874′, E110°48.209′, also known as “Daxiakou”) was located on the Western Yangtze Ramp, ~1000 km from the Meishan GSSP (Fig. 1B). It is estimated to have accumulated at water depths of ~200–300 m (Zhao et al., 2013). It contains the Upper Permian Dalong Formation and uppermost Permian to Lower Triassic Daye Formation, the contact between which is the LPME horizon (Fig. 2A). The Dalong Formation (Beds 223–251) consists mainly of black mudstone and shale (Fig. 2B) with scattered interbeds of marl and volcanic tuff (Fig. 2C–D). The overlying Daye Formation (Beds 252–280) consists mainly of gray mudstone and shale (Fig. 2E) with dozens of interbeds of volcanic tuff. The preservation of more numerous ash

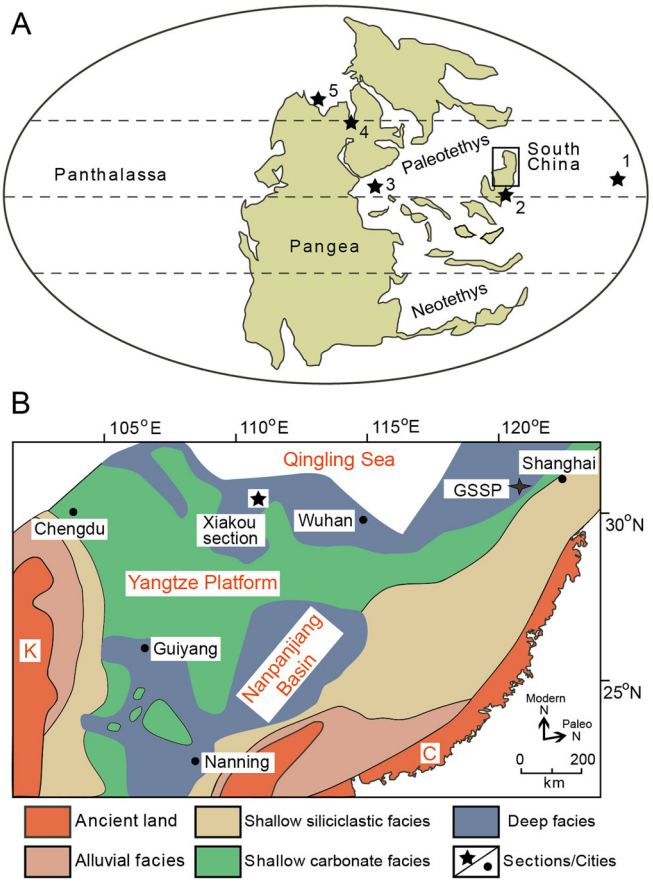

Fig. 1. (A) Global paleogeography at the Permian–Triassic boundary (~252 Ma). (B) Changhsingian paleogeography of the South China Craton (*Clarkina meishanensis* Zone; modified after Yin et al., 2014). GSSP = Global Stratotype Section and Point (Meishan D). Note locations of the Xiakou study section in B and global reference sections in A, including 1 = Ubara (Ayabe area, central Japan, Algeo et al., 2011), 2 = Nhi Tao (Cao Bang Province, Algeo et al., 2008), 3 = Bulla (Northern Italy, Gorjan et al., 2007), 4 = East Greenland (Fiskegrav, Greenland, Nielsen et al., 2010), and 5 = West Blind Fjord (Ellesmere Island, Canadian Arctic, Algeo et al., 2012). C = Cathaysia oldland; K = Kangdian oldland.

beds at Xiakou relative to many other PTB sections is probably related to its deeper-water setting, which resulted in more continuous sedimentation and less disruption or reworking of strata through physical or biological processes (Yin et al., 2014). Because the middle part of the study section straddling the LPME and PTB is exceptionally rich in tuffs (Beds 249–267), we have subdivided the 4.6-m-thick study section on this basis into Lower, Middle, and Upper units that correspond approximately to the pre-extinction, extinction, and post-extinction stages, respectively (Fig. 3).

Biostratigraphic study has identified four conodont zones at Xiakou (Wang and Xia, 2004; Zhao et al., 2013): (1) *Clarkina changxingensis changxingensis-C. deflecta* Zone, (2) *Hindeodus latidentatus-C. meishanensis* Zone, (3) *H. parvus* Zone, and (4) *Isarcicella isarcica* Zone, in ascending order (Fig. 3). Samples from the *H. latidentatus-C. meishanensis* Zone yielded a particularly diverse conodont assemblage, including *C. deflecta*, *C. postwangi*, *C. changxingensis changxingensis*, and *C. changxingensis yini* in addition to the zone’s eponymous species, constraining the position of the latest Permian mass extinction (LPME) horizon to the Bed 251/252 contact, a placement that is confirmed by the negative peak in $\delta^{13}C_{carb}$ at the base of Bed 252 (Fig. 3). The first appearance of the conodont *H. parvus*, which officially defines the PTB (Yin et al., 2001), was reported from the base of Bed 263 at Xiakou (Fig. 3). The base of the *I. isarcica* Zone, previously placed at

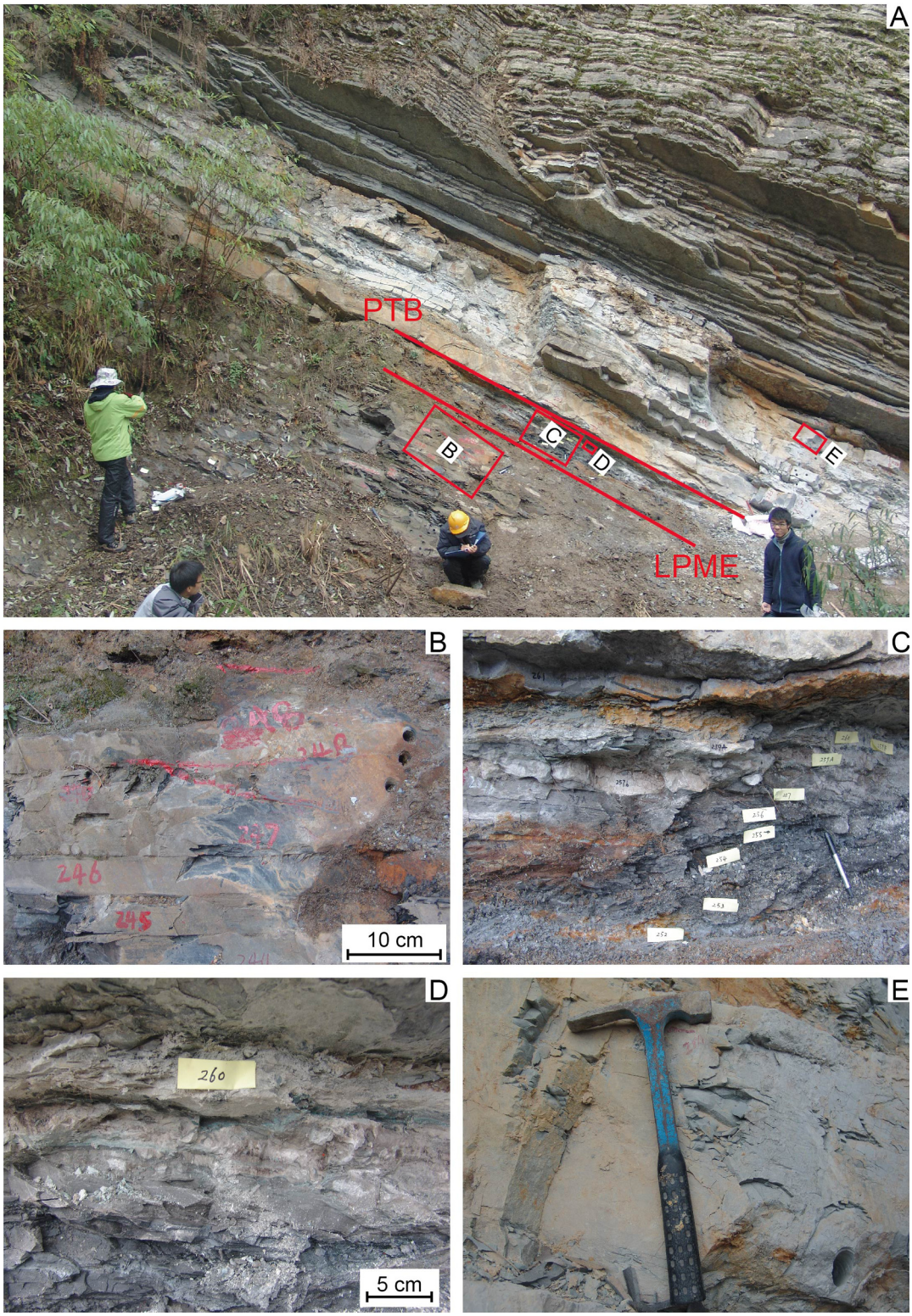

Fig. 2. Field photo of the Xiakou section (A); black mudstone of the Dalong Formation (B); black shale and volcanic ash interbeds between the LPME and PTB (C); detail of volcanic ash beds in the *C. meishanensis* Zone (D); and marl in the lower Daye Formation (E). The scale bars in A, C, and E are human, pen, and hammer, respectively.

the Bed 270/271 contact by Wang and Xia (2004), was recently reassigned to the Bed 266/267 contact by Zhao et al. (2013).

The Xiakou section can be readily correlated with the Meishan GSSP based on their conodont biostratigraphy and inorganic carbon isotope profiles (Fig. 3; Wang and Xia, 2004; Shen et al., 2012a; Zhao et al., 2013). The lower half of the *C. changxingensis-C. deflecta* Zone shows relatively uniform $\delta^{13}C_{carb}$ values, whereas the upper half exhibits a shift toward more negative values below the LPME horizon. A local $\delta^{13}C_{carb}$ minimum corresponding to Bed 246 at Xiakou and upper Bed 24d at Meishan may be correlative between the sections. Both profiles exhibit an abrupt excursion to a $\delta^{13}C_{carb}$ minimum at the LPME, followed by a

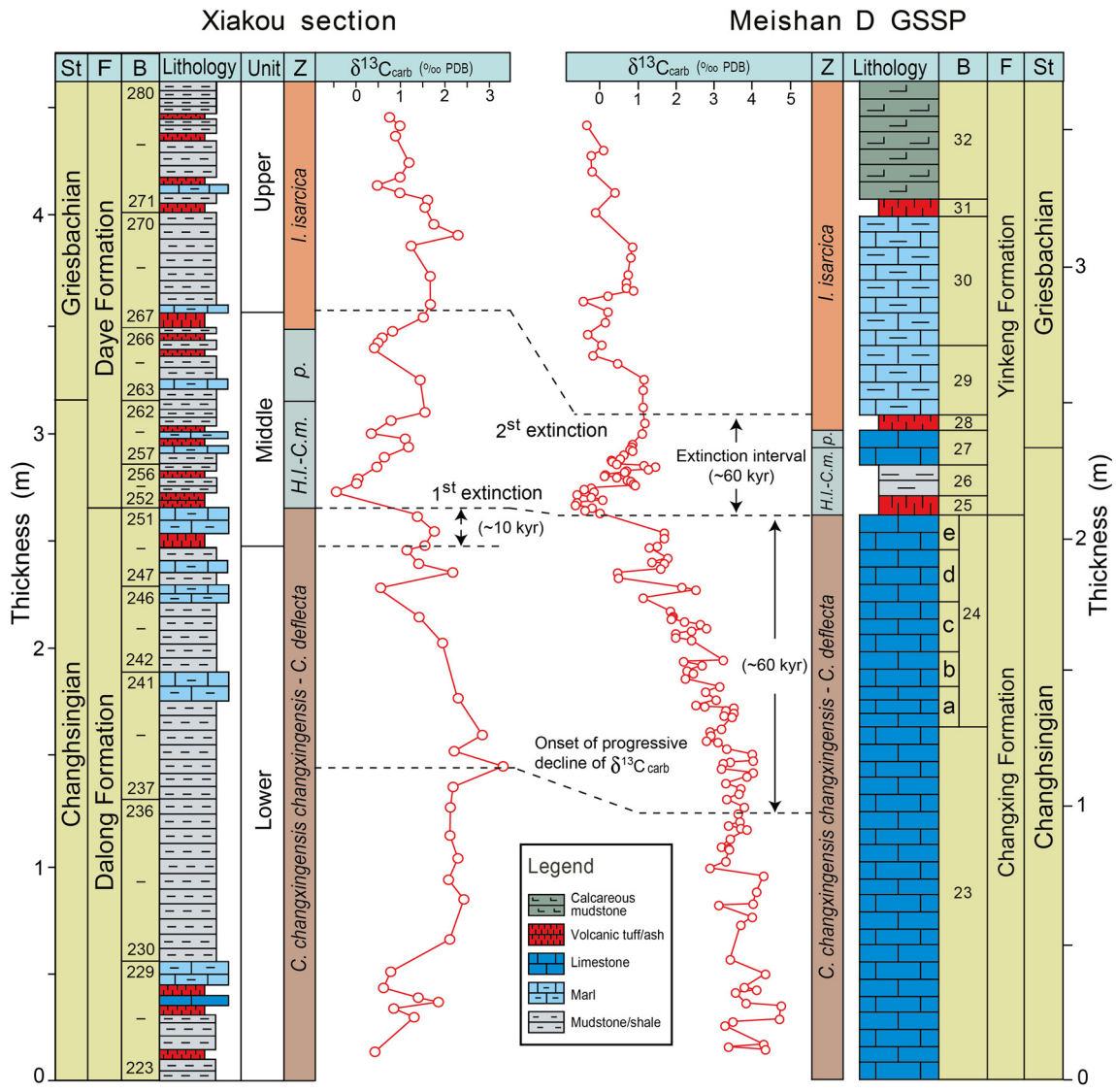

Fig. 3. Correlation of Xiakou with the Meishan GSSP. For Meishan, biostratigraphic data are from Yin et al. (2001), C-isotope data from Xie et al. (2007), and age data from Shen SZ et al. (2011) and Burgess et al. (2014). Abbreviations: *H.l.-C.m.* = *H. latidentatus-C. meishanensis* Zone; *p.* = *H. parvus* Zone; St = (sub)stage; F = formation; B = bed; Z = conodont zone. The Lower, Middle, and Upper units of the Xiakou section are based on lithological and geochemical differences, as discussed in the text.

recovery to more positive values within the *H. latidentatus-C. meishanensis* Zone. Moreover, the stratigraphic distribution of volcanic ash beds at Xiakou, which are concentrated in the *H. latidentatus-C. meishanensis* to lower *I. isarcica* zones, corresponds to that in the Meishan GSSP (Shen et al., 2012a, 2013a). This correlation framework demonstrates that the two extinction horizons at Xiakou (1st = Bed 252, 2nd = Bed 267) are correlative with the two main extinction horizons at Meishan D (Beds 25 and 28, respectively; Fig. 3).

The duration of the LPME to PTB interval has been estimated at ~60 kyr based on U–Pb dating of zircons (Shen SZ et al., 2011; Burgess et al., 2014, Fig. 3). At Xiakou, the mean linear sedimentation rate (LSR) between these horizons is ~15 m Myr^{-1}, which is substantially higher than that for the equivalent interval in the Meishan GSSP (3.5 m Myr^{-1}). The onset of the globally recognized carbonate δ^{13}C excursion began ~60 kyr (1.27 m) below the LPME at Meishan (Burgess et al., 2014). The onset of this gradual negative excursion can be recognized at ~1.2 m below the LPME at Xiakou (Fig. 3). These parameters yield a mean LSR of ~20 m Myr^{-1} for the pre-LPME upper Changhsingian at Xiakou, which is close to that of the correlative interval (Beds 22–25) at Meishan (26 m Myr^{-1}).

3. Material and methods

Numerous paleoceanic environmental proxies were used in this study to explore the oceanic environmental changes, including pyrite, iron speciation, and pyrite sulfur isotopes. For detailed descriptions refer to the Supplementary Material.

Our earlier studies at Xiakou were based on geochemical analysis of 68 samples from the 4.6-m-thick PTB interval (Shen et al., 2012a, 2013a). In this study, we selected subsets of these samples for analysis of Fe speciation (52 samples), pyrite sulfur isotopes (50 samples), and pyrite framboid size distributions (16 samples). Two or three polished blocks of each sample (3 cm × 3 cm) were made for *in situ* observation and measurement of pyrite framboids with a FEI Quanta 200 scanning electron microscope (SEM) at the State Key Laboratory of Geological Processes and Mineral Resources, China University of Geosciences (Wuhan). The spatial resolution of the secondary electron image of SEM is better than 3.5 μm. In backscattered electron (BSE) images, framboidal and euhedral crystal pyrites are easily distinguished by their shape and structure. The diameters of framboidal and euhedral pyrite crystals were measured directly on the SEM screen, with a precision of better than 0.1 μm. Although measurement of three-dimensional

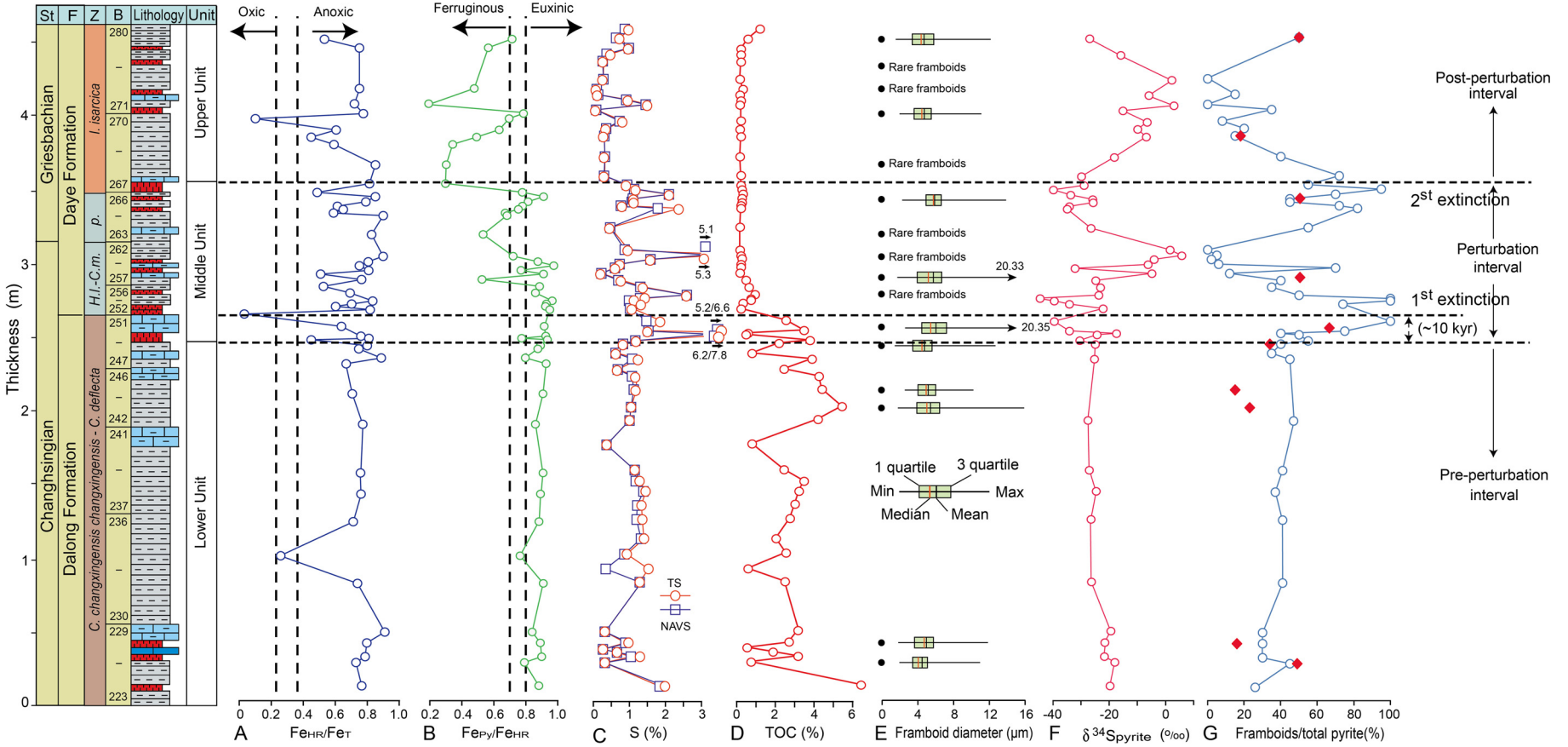

Fig. 4. Profiles of: (A) ratio of highly reactive Fe to total Fe (Fe_{HR}/Fe_T); (B) ratio of pyrite iron to highly reactive iron (Fe_{Py}/Fe_{HR}); (C) sulfur (S) (data from Shen et al., 2013a); (D) total organic carbon (TOC) (data from Shen et al., 2013a); (E) framboid diameter; (F) pyrite sulfur isotope ($\delta^{34}S_{pyrite}$); and (G) volume ratio of pyrite framboids to total pyrite (red diamonds = SEM data; open circles = S-isotope mixing model estimates). Note that $Fe_{HR} = Fe_{py} + Fe_{ox} + Fe_{mag} + Fe_{carb}$. The dashed lines in A and B are the thresholds for oxic versus anoxic (0.22–0.38) and ferruginous versus euxinic conditions (0.7–0.8; Poulton and Canfield, 2011), respectively. In C, TS = total sulfur; NAVS = non-acid-volatile sulfur; in E, Min = minima, Max = maxima. The 1st and 2nd extinctions are equivalent to Meishan D Beds 25 and 28, respectively. The duration of ~10 kyr below the LPME (1st extinction) is based on radiometric age data of Burgess et al. (2014). Other details as in Fig. 3.

spheres in two-dimensional images tends to underestimate their true diameter, the deviation from the true mean sphere diameter is generally <10% (Wilkin et al., 1996). The volume fraction of framboids to total pyrite was calculated as:

$$\text{Framboids/total pyrite (\%)} = \sum(4/3 \times 3.14 \times r_i^3)/\left[\sum(4/3 \times 3.14 \times r_i^3) + \sum R_j^3\right] \times 100 \quad (1)$$

where r_i, and R_j represent the radius (r, R) and number (i, j) of the framboidal and euhedral pyrite crystals in each sample, respectively. For each sample analyzed, from 173 to 703 individual pyrite crystals were measured.

Total pyrite concentrations and isotope compositions were analyzed using the chromium reduction method (Canfield et al., 1986). Pyrite extraction was performed under N_2 by the addition of 20 ml of 12N HCl together with 40 ml of 1 M chromous chloride solution. The reaction mixture was heated for 12 h, with the liberated sulfide collected as silver sulfide after bubbling through 30 ml of 3 wt% silver nitrate solution with 10% NH_4OH by volume (for isotopic analysis). Mean recovery of replicate pure pyrite standards was 99.5%. Filtered, rinsed, and dried Ag_2S precipitates were combined with an excess of V_2O_5 and analyzed for S-isotope composition following online combustion using a Thermo Instruments Delta V Plus isotope ratio mass spectrometer coupled with a Costech elemental analyzer at the University of California, Riverside. Sulfur isotope compositions were calculated as $\delta^{34}S = (R_{sample}/R_{standard} - 1) \times 1000$, where R is the ratio of $^{34}S/^{32}S$, and reported as per mille (‰) deviations from the V-CDT international standard. The analytical error was ~0.1‰ (1σ), calculated from replicate analyses of IAEA international standards. Samples were calibrated using the same international standards: IAEA S1 (−0.3‰), IAEA S2 (+22.65‰) and IAEA S3 (−32.5‰). To determine concentrations of pyrite S, the Ag_2S precipitates were acidified with 10 ml of 6 M HCl to re-liberate the sulfur, followed by titration with a 0.1 M KIO_3 solution in the presence of excess KI and starch.

The iron content associated with pyrite (Fe_{py}) in rock samples was calculated stoichiometrically based on the pyrite sulfur concentrations obtained from the foregoing procedure. Fe_{carb}, Fe_{ox} and Fe_{mag} were measured using the following sequential extraction procedure (Poulton and Canfield, 2005) starting with 100 mg of powdered sample in a 15-ml sterile centrifuge tube. First, Fe_{carb} was extracted in a 50 °C water bath for 48 h with shaking using 1 M sodium acetate solution adjusted to pH = 4.5 by addition of trace-metal grade acetic acid. Second, Fe_{ox} was extracted from the same residue using a 50 $g\,L^{-1}$ sodium dithionite solution buffered to pH = 4.8 with 0.2-M sodium citrate and trace-metal grade acetic acid in room temperature water bath for 2 h with shaking. Finally, Fe_{mag} was extracted from the second-step residue using a 0.2-M ammonium oxalate/0.17-M oxalic acid solution in room temperature water bath for 6 h with shaking. Between each extraction step, the sample was centrifuged to remove the supernatant. All extracts were diluted 100-fold in 2% nitric acid and analyzed for their Fe contents on a quadrupole ICP-MS at State Key Laboratory of Biogeology and Environmental Geology, China University of Geosciences (Wuhan). The reproducibility of the iron extraction data is given in Table S1.

4. Results and redox interpretations

Nearly all study samples yield ratios of highly reactive iron to total iron (Fe_{HR}/Fe_T) that are >0.4, consistent with generally anoxic depositional conditions (Fig. 4A; note one oxic outlier each in the Lower and Upper units). Mean Fe_{HR}/Fe_T ratios for all three

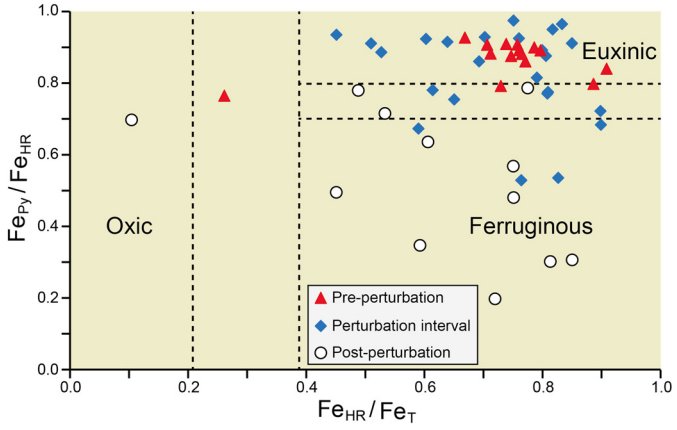

Fig. 5. Crossplots of ratio of highly reactive Fe to total Fe (Fe_{HR}/Fe_T) to ratio of pyrite iron to highly reactive iron (Fe_{Py}/Fe_{HR}). The thresholds for oxic versus anoxic (0.22–0.38) and ferruginous versus euxinic conditions (0.7–0.8) are from Poulton and Canfield (2011). Other details as in Fig. 4.

units are similar (~0.7), although the Lower Unit exhibits distinctly less sample-to-sample variation than the Middle and Upper units. In contrast, Fe_{Py}/Fe_{HR} ratios are distinctly different in the three units (Fig. 4B): the Lower Unit exhibits relatively uniform values of 0.8–0.9, the Middle Unit exhibits moderately variable values of 0.5–1.0, and the Upper Unit exhibits highly variable values of 0.2–0.8. The generally high Fe_{Py}/Fe_{HR} ratios of the Lower and Middle units suggest mainly euxinic depositional conditions, possibly with fluctuations to ferruginous conditions in the Middle Unit. However, persistently high ratios are unlikely to have been due to diagenetic pyrite formation (Poulton and Canfield, 2005). The lower and more variable Fe_{Py}/Fe_{HR} ratios of the Upper Unit suggest mainly ferruginous depositional conditions, possibly with fluctuations to euxinia. Alternatively, the locally high Fe_{Py}/Fe_{HR} ratios of the Upper Unit may reflect later development of porewater euxinia. Fig. 5 shows the Fe-speciation relationships among Lower, Middle, and Upper unit samples, confirming the shift from dominantly euxinic conditions in the pre-extinction Upper Permian to dominantly ferruginous conditions in the lowermost Triassic.

Total sulfur (TS) exhibits slightly higher mean values in the Lower Unit (1.5 ± 1.6%) than in the Middle and Upper units (1.0 ± 1.9%; Fig. 4C). However, the highest TS values (>5%) are found at the base and top of the Middle Unit. The distribution of non-acid-volatile sulfur (NAVS) is almost identical to that of TS, with concentrations equal to 90–95% of TS in most samples. These relationships demonstrate that most sulfur in the study section belongs to the non-acid-volatile fraction and, thus, is resident in either organic matter (S_{org}) or pyrite (S_{py}). Total organic carbon (TOC) concentrations are high in the Lower Unit (2.67 ± 1.49%), but markedly lower in the upper two units (0.32 ± 0.24%) (Fig. 4D).

Pyrite is found throughout the study section in the form of framboids and euhedral crystals. In the Lower Unit, all five samples yielded abundant framboids that are small (<8 μm) and show limited size variation (Fig. 6A–B). In the Middle Unit, half of the samples (three out of six) contained abundant small framboids (mean values were lower than 5.75 μm, Fig. 6C), whereas the others have relatively fewer framboids (Fig. 6D). The high Fe content of Middle Unit samples appears to be due not to pyrite content but, rather, to Fe-rich volcanic ash layers. In the Upper Unit, two of five samples contained abundant small framboids (Fig. 6E). Small amounts of euhedral pyrite crystals are present in all samples, including those lacking framboidal pyrite (Fig. 6F).

The 16 study samples analyzed petrographically yielded a total of 4178 pyrite framboids whose size distributions (Fig. 7) are sum-

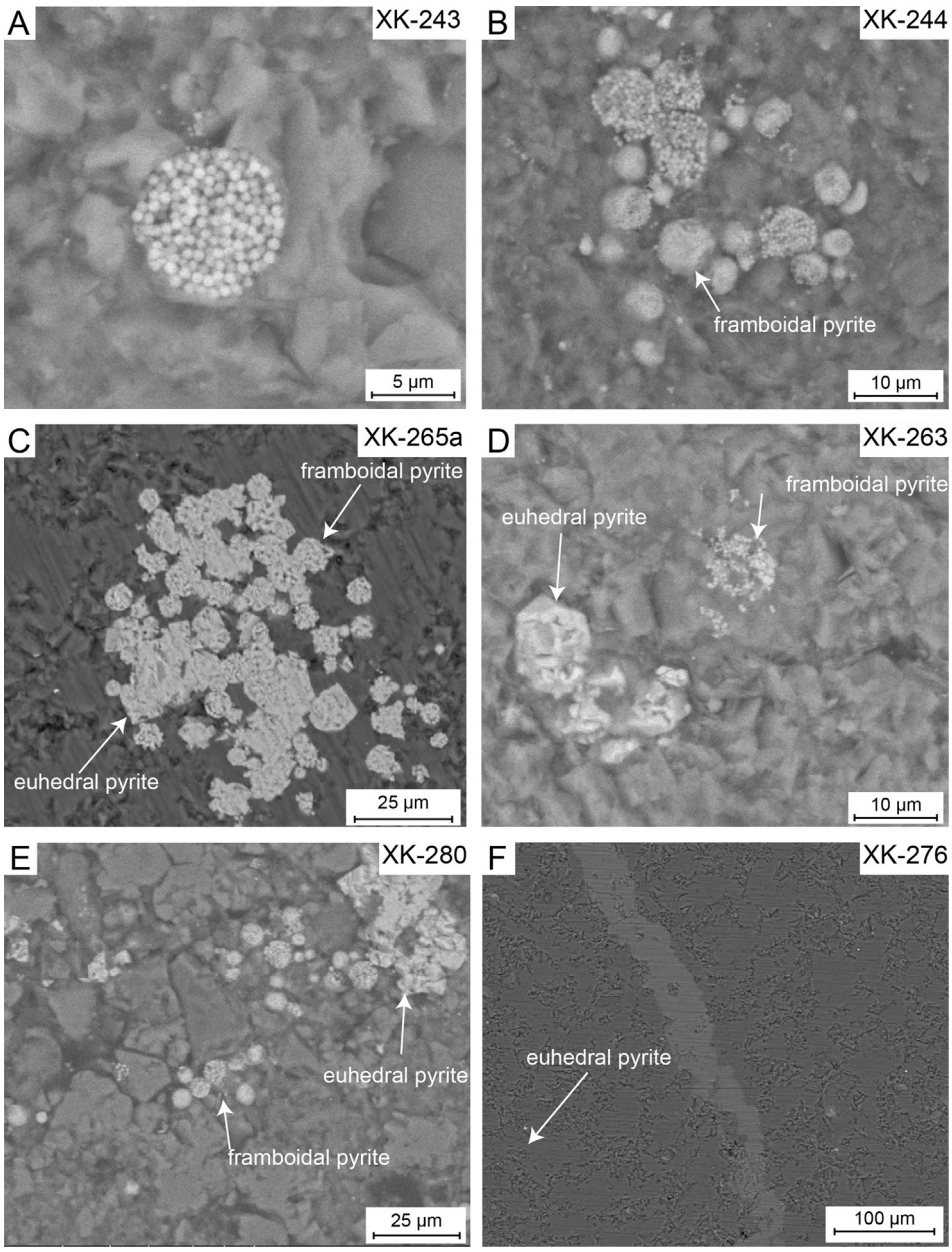

Fig. 6. Backscattered electron (BSE) images of (A) typical pyrite framboid (Sample XK-243); (B) abundant framboids with a few euhedral crystals (Sample XK-244); (C) co-occurring framboids and euhedral crystals (Sample XK-265a); (D) euhedral pyrite crystals with a few framboids (Sample XK-263); (E) abundant framboids with some euhedral crystals (Sample XK-280), and (F) rare framboids with a few euhedral pyrite crystals (Sample XK-276).

marized with box-and-whisker plots (Fig. 4E). The mean sizes of framboids vary little between samples, clustering around 4–5 μm, with standard deviations mostly <2 μm and skewness <2. The maximum framboid diameters are <13 μm for all samples except XK-243 (16 μm), XK-250 (20 μm), and XK-257a (20 μm). No systematic stratigraphic variation in pyrite framboid sizes was observed (Fig. 4E). See Table S2 for a summary of framboid size measurements.

Pyrite S isotope ($\delta^{34}S_{pyrite}$) values vary strongly within the study section (Fig. 4F). The Lower Unit shows relatively uniform $\delta^{34}S_{pyrite}$ values of -23.66 ± 3.28‰. The Middle Unit is characterized by large fluctuations ranging from -45.52‰ to $+21.96$‰, with an average of -24.84‰. Two prominent negative peaks were recorded near the base (lower *C. meishanensis* Zone) and top (upper *H. parvus* Zone) of the Middle Unit. The middle part of the Middle Unit as well as most of the Upper Unit is characterized by relatively heavy $\delta^{34}S_{pyrite}$ (-10‰ to $+10$‰).

5. Discussion

5.1. Syngenetic versus diagenetic pyrite

The presence and amount of syngenetic framboidal pyrite formed in the water column provides information about water-mass redox conditions (Wilkin et al., 1996). Measurements from modern marine systems provide a guide for assessing whether framboids are syngenetic or diagenetic in origin based on the mean and standard deviation of framboid diameters. At Xiakou, the generally small mean sizes (4–5 μm) and standard deviations (<2 μm) of framboids are consistent with a predominantly syngenetic origin (Figs. 4E, 7). Sporadic larger framboids may represent diagenetic growths or overgrowths on earlier-formed syngenetic framboids, as suggested by visible overgrowths on some individual crystals (Fig. 6C). Fluctuations in porewater redox conditions (e.g., due to downward penetration of oxy-

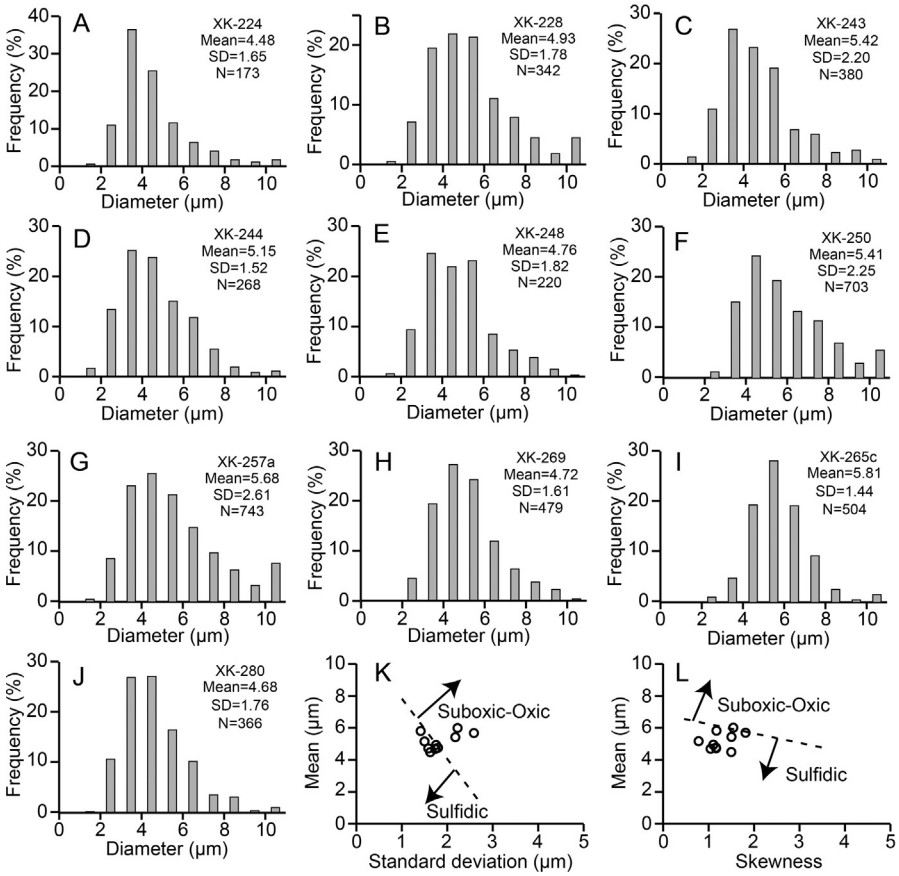

Fig. 7. (A)–(J) Size distributions of pyrite framboids by sample. Horizontal and vertical axes represent framboid diameter (μm) and relatively frequency (%) respectively. (K) Mean diameter (μm) versus standard deviation (μm), and (L) Mean diameter (μm) versus Skewness of framboids for all samples. The dashed line separates euxinic from suboxic–oxic conditions (cf. Wilkin et al., 1996). SD = standard deviation; for other details, see Table S2.

gen into the sediment) can cause oxidation of hydrogen sulfide followed by secondary MSR, yielding a mixture of syngenetic and diagenetic pyrite in the sediment (e.g., Wilkin et al., 1996; Riccardi et al., 2006). This combination of processes thus may produce a complicated record of pyrite morphologies and S isotopic compositions.

Most samples show evidence of containing a mixture of syngenetic framboidal pyrite and diagenetic euhedral pyrite. The proportion of total pyrite comprised of syngenetic framboids (Fig. 4G) was estimated by two independent, complementary methods. First, the frequency and size of both framboidal and euhedral crystals was measured in SEM images of 16 samples (e.g., Fig. 6), and the total volume of each type was calculated per Eq. (1). Second, the syngenetic framboidal content of 48 samples analyzed for pyrite $\delta^{34}S$ was estimated based on a S-isotope model (modified from Algeo et al., 2008). In this model, a variable fraction of syngenetic pyrite with a strongly ^{34}S-depleted composition (here estimated at $-42‰$) mixed with a small fixed fraction of late-stage diagenetic pyrite with a ^{34}S-enriched composition (here estimated at 0.1% pyrite S with a $\delta^{34}S$ of 0‰; red line, Fig. 8) was used. Variance to the right of this mixing trend was interpreted as evidence of a third component, i.e., early-diagenetic pyrite that is ^{34}S-enriched owing to Rayleigh distillation of porewater sulfate. We modeled this early-stage pyrite addition for each sample (representative mixing trends are shown by dashed lines labeled I–III, Fig. 8) and then calculated the amount of syngenetic pyrite as a function of these three pyrite fractions (Table S3). The results of this S-isotope model are in good agreement with the SEM data: of ten samples analyzed by both methods, four (at 0.20, 2.45, 3.44, 3.85 and 4.50 m) yielded nearly identical estimates of the amounts of syngenetic pyrite, and three samples (at 0.35, 2.00, 2.20, 2.54 and 2.88 m) yielded slightly higher estimates for the S-isotope model than for the SEM analysis (Fig. 4G). Pyrite in the Lower Unit consists of 30–40% syngenetic framboids on average, the base and the top of the Middle Unit are characterized by sharp shifts to greater amounts of syngenetic pyrite (70–100%), and the middle part of the Middle Unit as well as the Upper Unit is characterized by lesser amounts of syngenetic pyrite (mostly <30%; Fig. 4G).

5.2. Redox variation at Xiakou

Widespread oceanic anoxia is thought to have been one of the most important causes of the PTB mass extinction (Wignall and Twitchett, 1996; Grice et al., 2005). Global deep-ocean anoxia throughout the Late Permian to Early Triassic (~10 Myr) was proposed by Isozaki (1997), although recent geochemical (Algeo et al., 2011) and modeling studies (Winguth and Winguth, 2012) have shown that the deep ocean was mainly suboxic during the PTB crisis, and that oceanic anoxia developed mainly through expansion of intermediate-depth oxygen minimum zones. The resulting upward chemocline excursions (e.g., Kump et al., 2005) probably led to widespread development of photic-zone euxinia, as documented by biomarker evidence (Grice et al., 2005; Xie et al., 2005, 2007). Upward chemocline excursions also affected the planktonic community, triggering the disappearance of deepwater radiolarians (Shen et al., 2012b). One consequence of these excursions was that shallow-water settings experienced frequent shifts between oxic and anoxic/dysoxic conditions during the latest Permian to Early Triassic (Bond and Wignall, 2010). However, there is no consensus yet regarding the specifics of spatial and temporal redox variation during the PTB crisis.

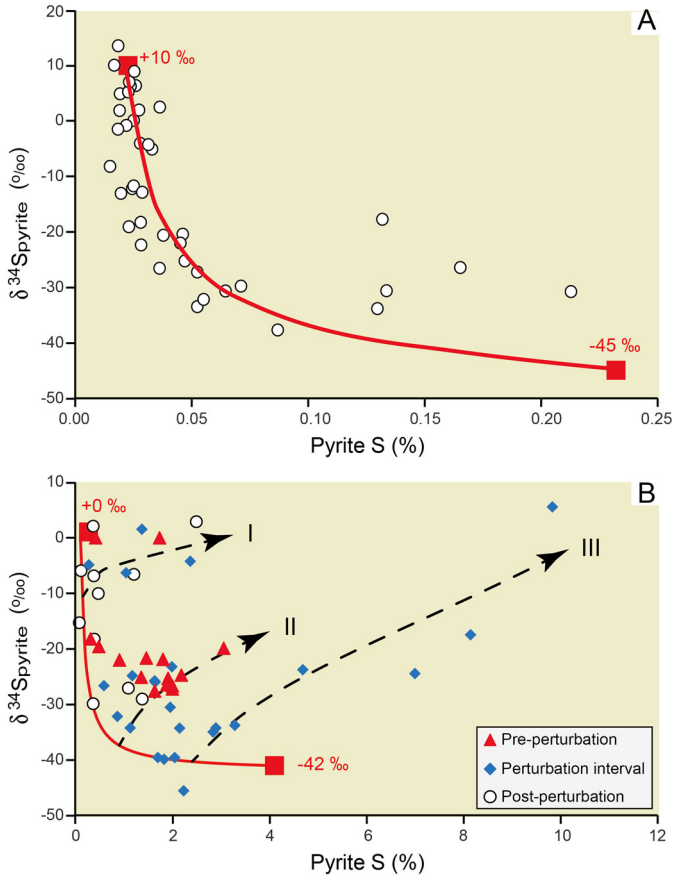

Fig. 8. $\delta^{34}S_{Py}$ versus pyrite S concentration. (A) PTB section at Nhi Tao, Vietnam (from Algeo et al., 2008, their Fig. 4). Note that most $\delta^{34}S_{Py}$ variance is explained by two-component mixing between low-S (late diagenetic) and high-S (syngenetic) endmembers having $\delta^{34}S = +10\%$ and -45%, respectively. (B) The Xiakou study section. The red curve represents a two-component mixing model between low-S and high-S endmembers having $\delta^{34}S = +0\%$ and -42%, respectively. The dashed lines I, II, and III represent additions of an early-diagenetic component in a partially closed system influenced by Rayleigh distillation; see text for discussion. (For interpretation of the references to color in this figure legend, the reader is referred to the web version of this article.)

In this study, local redox changes can be clearly demonstrated through the integration of Fe and S data. The Lower Unit (pre-extinction interval) was characterized by predominantly euxinic conditions, as shown by several proxies including high ratios of Fe_{HR}/Fe_T (>0.7) and Fe_{Py}/Fe_{HR} (>0.7) (Figs. 4A–B, 5), the presence of syngenetic pyrite framboids in all samples (Fig. 4E), and nearly uniform, strongly ^{34}S-depleted pyrite S-isotope compositions (Fig. 4F). High concentrations of redox-sensitive trace-metal concentrations (e.g., Mo, U, and V) in the Lower Unit are also consistent with euxinic conditions (Shen et al., 2013a). The lack of variation of most proxies in vertical profile through the Lower Unit is a reflection of the relative stability of oceanic conditions during the pre-LPME interval of the Late Permian. However, this stability ended abruptly ~18 cm below the LPME, reflecting the onset of major oceanic perturbations prior to the 1st extinction horizon (Fig. 4; see Section 5.6).

The Middle Unit (extinction interval) was characterized by strongly fluctuating redox conditions. These conditions were mostly anoxic (based on $Fe_{HR}/Fe_T > 0.4$), with euxinia in the lower half of the Middle Unit (based on $Fe_{Py}/Fe_{HR} > 0.7$) and variably euxinic to ferruginous conditions in the upper half of this unit (based on strong variation in Fe_{Py}/Fe_{HR}). Frequent perturbations appear to have resulted in an unsettled marine environment at that time, as reflected in multiple spikes in TS (Fig. 4C) and Mo, U, and V (Shen et al., 2013a), and in large, rapid changes in pyrite framboid abundance and pyrite S-isotopic composition (Fig. 4F–G).

The Upper Unit (post-extinction interval) was characterized by predominantly ferruginous conditions that were punctuated by possible sporadic euxinic episodes. These conditions are indicated by a combination of high Fe_{HR}/Fe_T (>0.4) and low Fe_{Py}/Fe_{HR} (<0.7) values, although with sporadic increases in Fe_{Py}/Fe_{HR} to >0.7 (Fig. 4A–B). The relative infrequency of euxinic conditions is reflected in declines in TS (Fig. 4C), TOC (Fig. 4D) and pyrite framboid abundance (Fig. 4G) and an increase in pyrite $\delta^{34}S$ values (Fig. 4F), suggesting that a greater proportion of total pyrite formed diagenetically within the sediment. Sharply reduced concentrations of TOC, Mo, U, and V (Fig. 4D, Shen et al., 2013a) are also consistent with limited euxinia. Although some proxies continue to show large fluctuations in vertical profile, the frequency and size of such fluctuations appear reduced compared to the Middle Unit (Fig. 4), suggesting that the intensity of oceanic perturbations diminished somewhat in the post-extinction interval.

5.3. Depth-dependent marine redox changes during the Permian–Triassic transition

The record of changing oceanic environmental conditions during the Permian–Triassic transition can be tracked through analysis of pyrite S-isotope records globally. Shifts toward lighter $\delta^{34}S_{py}$ compositions are generally associated with greater inputs of syngenetically formed pyrite framboids to the sediment and, thus, with expansion of water-column euxinia. Given a Late Permian seawater sulfate $\delta^{34}S$ of ca. +10‰ to +15‰ (Song et al., 2014), pyrite $\delta^{34}S$ compositions of ca. −30‰ or lower are suggestive of maximum fractionation during MSR, as commonly observed in the water column of anoxic marine systems.

For PTB sections with high-resolution pyrite S-isotope profiles, changes in $\delta^{34}S_{py}$ appear to be strongly linked to water depth (Fig. 9). Shallow-water sections such as Bulla and Nhi Tao show relatively heavy $\delta^{34}S_{py}$ below the LPME, reflecting mainly diagenetic pyrite formation, and abrupt but transient shifts to lighter $\delta^{34}S_{py}$ at/above the LPME, reflecting brief sulfidic episodes (Fig. 9A–B; Gorjan et al., 2007; Algeo et al., 2008). The brevity of these negative $\delta^{34}S_{py}$ excursions suggests a transient influx of H_2S into the ocean-surface layer, as during a chemocline upward excursion (Kump et al., 2005), with subsequent rapid oxidation of the H_2S to sulfate. The close association of the first of these sulfidic events at Bulla and Nhi Tao with the LPME horizon is at least circumstantial evidence that H_2S toxicity was an important factor in the demise of shallow-marine benthic communities during the PTB crisis (Algeo et al., 2008).

Intermediate-depth sections such as Meishan, West Blind Fiord, and Greenland exhibit shifts toward lighter $\delta^{34}S_{py}$ well below the LPME and persistently light $\delta^{34}S_{py}$ into the Early Triassic (Fig. 9C–E; Nielsen et al., 2010; Shen YA et al., 2011; Algeo et al., 2012). This pattern suggests a widespread expansion of oceanic oxygen-minimum zones prior to the mass extinction event, most probably due to incipient warming of the ocean-surface layer and intensified water-column stratification (Winguth and Winguth, 2012; Song HY et al., 2013). The biotic effects of expanded oceanic anoxia prior to the LPME are seen in a reduction in deepwater sponge spicule size (Liu et al., 2013), the regional loss of deepwater sponge communities (Algeo et al., 2012), and the extinction of deepwater radiolarians (i.e., the Albaillellaria and Latentifistularia) (Shen et al., 2012b). These patterns are consistent with a gradual expansion of oceanic oxygen-minimum zones during the latest Permian.

Deepwater sections such as Xiakou and Ubara also show generally light $\delta^{34}S_{py}$ during the latest Permian and into the Early Triassic (Fig. 9F–G; Algeo et al., 2011; this study). Persistently euxinic

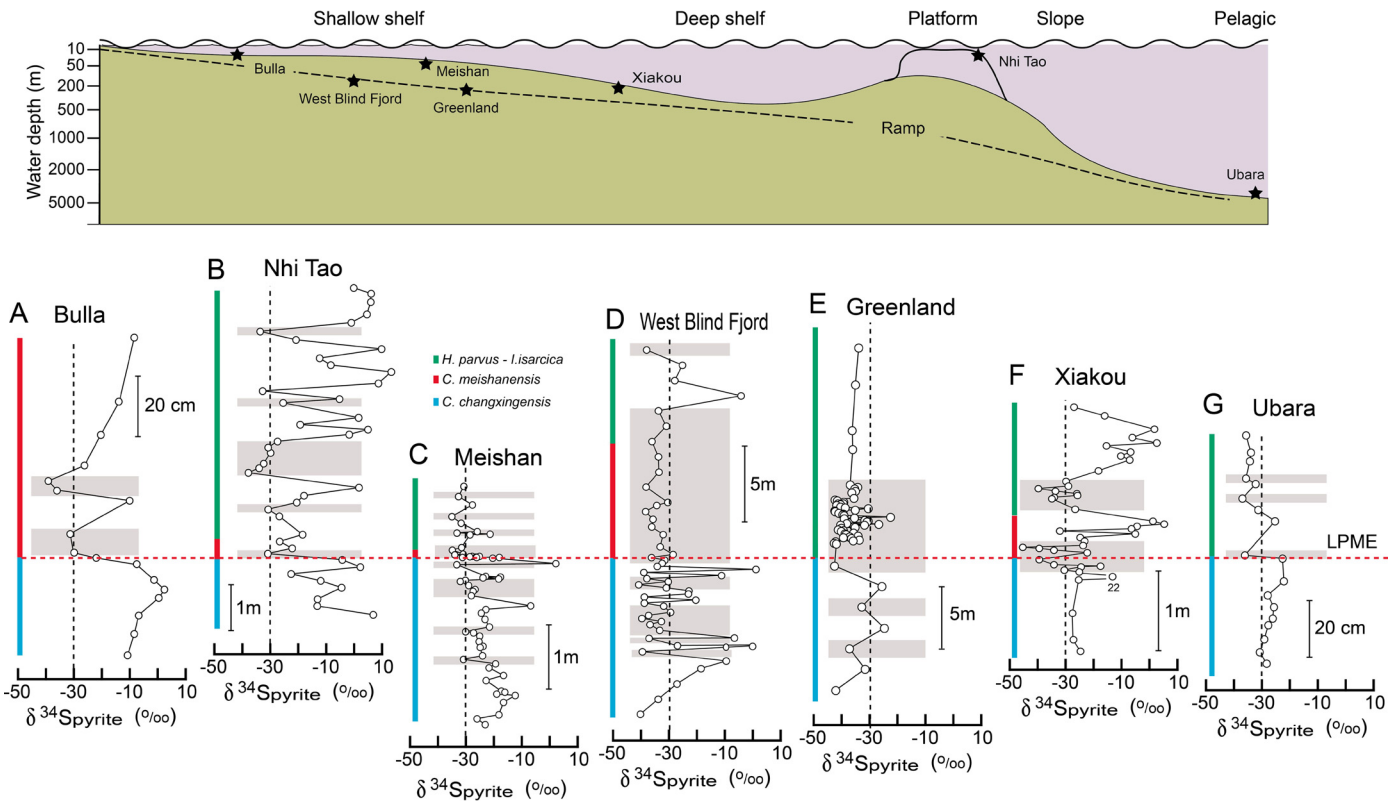

Fig. 9. The upper part is the location of study sections within a generalized depositional profile. The lower part are profiles of $\delta^{34}S_{pyrite}$ from Bulla section (Gorjan et al., 2007), Nhi Tao section (Algeo et al., 2008), Meishan section (Shen YA et al., 2011), West Blind Fjord (Algeo et al., 2012), Greenland (Nielsen et al., 2010), and Ubara (Algeo et al., 2011). The shaded fields highlight the negative excursions in each section with −30‰ (dashed line) for reference. Ubara lacks a detailed conodont biozonation. The red dash line means the Latest Permian mass extinction (LPME). For section locations see Fig. 1. Note that the vertical scales are different for each section. (For interpretation of the references to color in this figure legend, the reader is referred to the web version of this article.)

conditions in the pre-extinction interval at Xiakou appear to have been destabilized by the LPME event, resulting in fluctuations between ferruginous and euxinic conditions although with transient oxic-suboxic episodes following the 1st mass extinction (see Section 5.2). The development of ferruginous anoxic conditions during deposition of portions of the Middle and Upper units might suggest a strong drawdown of the seawater sulfate reservoir due to expanded anoxia and widespread pyrite burial. Luo et al. (2010) estimated that seawater sulfate was drawn down to 3–15% of its present-day concentration during the Early Triassic. The geographic extent of ferruginous conditions during the Permian–Triassic transition remains unclear owing to the paucity of Fe-speciation studies of other PTB sections. The only other study of this type to date documented mainly anoxic ($Fe_{HR}/Fe_T = 0.6 \pm 0.2$), ferruginous ($Fe_{Py}/Fe_{HR} = 0.4 \pm 0.3$) conditions at Shangsi (NW China) within the stratigraphic equivalent of the present study interval (Xiang et al., 2016). It is possible that drawdown of sulfate was regionally greater in South China than elsewhere. If so, a likely cause of such spatially variable drawdown was intense volcanic activity around the margins of the South China Craton, delivering large quantities of highly reactive Fe to marine sediments and thus locally tipping the system from euxinic to ferruginous conditions.

The Ubara section shows light $\delta^{34}S_{py}$ prior to the LPME (Fig. 9G), although the near-absence of organic matter in its Upper Permian radiolarites prevented porewater MSR, leading to an isotopic signature influenced by small quantities of syngenetic framboidal pyrite. This section records a large increase in the flux of framboidal pyrite to the sediment at the LPME, signaling a major expansion of euxinia within the overlying oxygen-minimum zone (Algeo et al., 2011). In contrast, the deep Panthalassic Ocean remained suboxic throughout the Permian–Triassic transition, as indicated by negligible changes in the flux of authigenic redox-sensitive trace metals to the sediment (Algeo et al., 2011) and by global paleoceanographic modeling results (Winguth and Winguth, 2012).

5.4. Two pulses of oceanic disturbance during the PTB crisis

Patterns of biotic change during the Permian–Triassic transition have become better known in recent years through detailed biostratigraphic studies. Jin et al. (2000) documented an abrupt, single-phase mass extinction event of latest Permian age in Bed 25 of the Meishan GSSP. Subsequent studies have established that this 1st extinction event was followed by a 2nd event of earliest Triassic age, correlative with Bed 28 at Meishan, that was smaller in absolute numbers but as large in terms of extinction magnitude (i.e., percentage of extant taxa lost) (Yin et al., 2012). In the most comprehensive study to date, Song HJ et al. (2013) analyzed the ranges of 537 species in seven Chinese sections, concluding that the extinction rate of the 2nd event was higher (71%) than that of the 1st event (57%) (Fig. 10A). Each of these two events was preceded by a minimum and followed by a maximum in the abundance ratio of cyanobacterial biomarkers to general bacterial biomarkers (2-methylhopane or 2-MHP index), reflecting the microbial community response to these bioevents (Fig. 10B; Xie et al., 2005, 2007). A two-phase Permian–Triassic biocrisis now appears well-established.

There is less consensus regarding patterns of environmental change during the Permian–Triassic transition. A number of high-resolution studies have documented two negative peaks in carbonate $\delta^{13}C$ globally (see Korte and Kozur, 2010, and references therein), especially in deepwater sections, whereas only a single

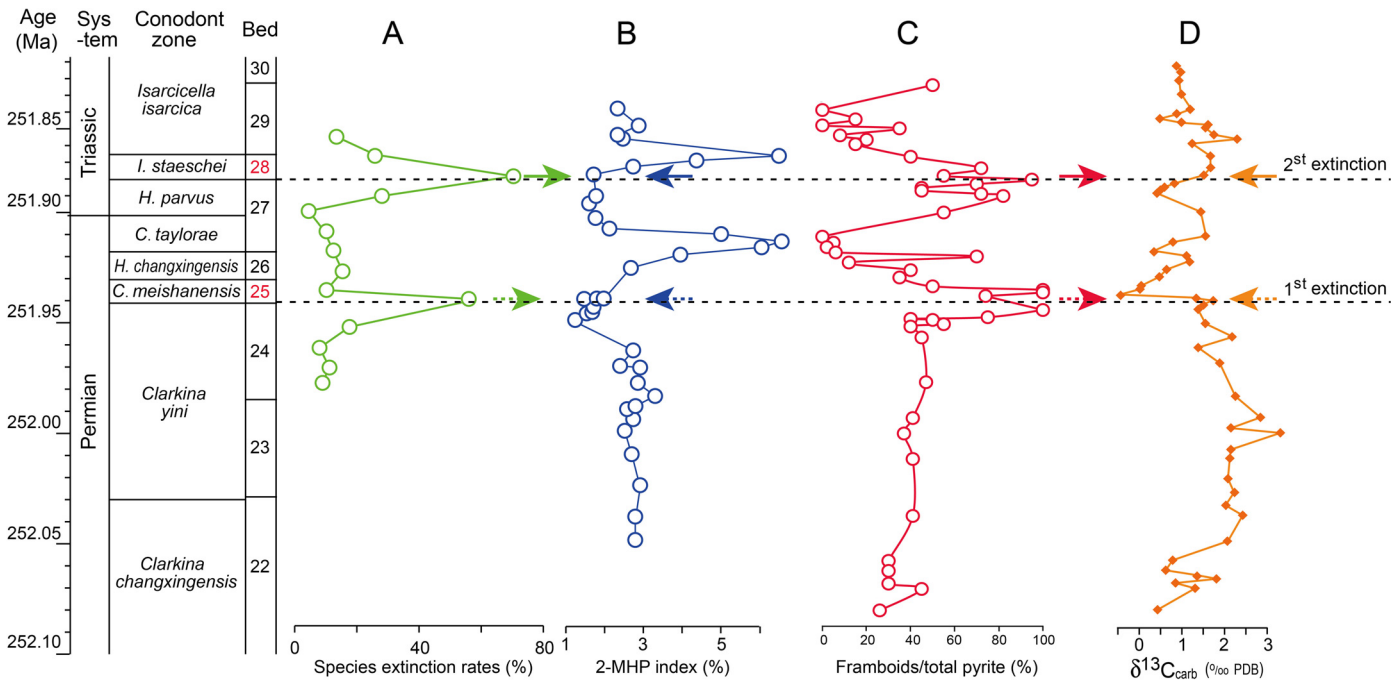

Fig. 10. Profiles of (A) Species extinction rates at Meishan (Song HJ et al., 2013); (B) 2-methylhopane (2-MPH) at Meishan (Xie et al., 2005); (C) volume ratio of framboids to total pyrite at Xiakou (this study); and (D) carbonate $\delta^{13}C$ at Xiakou (Shen et al., 2012a). Beds 25 and 28 represent volcanic ash layers at Meishan that coincide with the 1st and 2nd extinction events; the pattern of geochemical shifts associated with these horizons is shown by arrows. Age data are from Shen SZ et al. (2011), Shen YA et al. (2011) and Burgess et al. (2014). Conodont zone and bed number for Meishan D are from Yin et al. (2014). Other details as in Figs. 2 and 4.

excursion has been reported from many shallow-water sections, in which an unconformity is commonly present owing to latest Permian eustatic regression (Yin et al., 2014). The Meishan GSSP has been inferred to record two protracted cycles of oceanic perturbation, the first from Bed 23 to Bed 28 and the second from Bed 29 to Bed 39 (Xie et al., 2007; Yin et al., 2012). Each cycle is characterized by successive stages of oscillatory deterioration, a crisis peak, and post-crisis amelioration, with the crisis peaks corresponding to minima in the carbonate carbon isotope profile and with deposition of volcanic ash layers (Beds 25 and 28). The two biocrisis horizons generally correlate with the thickest volcanic ash depositions in both shallow- and deepwater sections (e.g., Dongpan and Xinmin sections in the south part of the South China Craton; Shen et al., 2012b, 2013b).

The Xiakou section shows multiple negative $\delta^{13}C_{carb}$ excursions within the Permian–Triassic transition interval, all of which appear to have been linked to volcanic eruptions, as recorded by thick (>2 cm) ash layers (Fig. 10C). The two largest $\delta^{13}C_{carb}$ excursions are associated with 20- to 25-cm-thick composite tuffs in Beds 249–252 and 265–267 that have been correlated with Meishan Beds 25 and 28, respectively, and, thus, with the two $\delta^{13}C_{carb}$ excursions observed in other PTB sections globally (Fig. 3; Shen et al., 2012a). These two large volcanic events in the Xiakou section show a pronounced relationship to the Fe–S proxies of the present study (Fig. 10D). Each event is associated with a large increase in TS (Fig. 4C) and framboid abundance (Fig. 4F), sustained or increased Fe_{Py}/Fe_{HR} (Fig. 4B), and a shift toward lower $\delta^{34}S_{py}$ values (Fig. 4E), characteristics that are indicative of euxinic bottomwater conditions. In contrast, the beds within the Middle Unit that are between these tuffaceous intervals are associated with mostly ferruginous conditions. This pattern suggests that ferruginous conditions were the norm during the crisis interval, but that euxinic conditions developed in conjunction with each episode of intensified volcanic activity.

5.5. Volcanic trigger of oceanic perturbations during the PTB crisis?

Several lines of evidence suggest that volcanic eruptions were the trigger for oceanic perturbations during the PTB crisis. First, the onset of strong fluctuations in multiple geochemical profiles at Xiakou (including $\delta^{34}S_{py}$, $\delta^{13}C_{carb}$, framboids, Mo, U, V; Figs. 3–4) coincided with initial deposition of the ~24-cm-thick composite ash layer of Beds 249–252. Second, large geochemical excursions higher in the study section (Middle and Upper units) were commonly associated with other thick ash layers (Fig. 4). The magnitudes of $\delta^{13}C_{carb}$ excursions exhibit a good correlation with the thicknesses of the volcanic ash beds, suggesting that the intensity of oceanic environmental perturbations scaled with eruption size (Shen et al., 2012a). Similar relationships between oceanic environmental conditions (e.g., redox, productivity, and terrigenous inputs) and volcanic ash layers have been established for other deepwater sections of the Nanpanjiang Basin, e.g., Dongpan and Xinmin (Shen et al., 2012b).

The exact connection between volcanic activity and negative $\delta^{13}C_{carb}$ excursions in PTB sections is uncertain, with either a direct volcanic or an indirect oceanic cause being possible. Previous studies have suggested that volcanism released isotopically light C and S due to magmatic outgassing or to subsurface baking of organic matter by magmatic intrusions, yielding thermogenic methane and sulfur dioxide (Retallack and Jahren, 2008; Svensen et al., 2009). Subsequently, acid precipitation may have increased subaerial chemical weathering rates, leading to increased nutrient and sulfur fluxes to the ocean (Algeo and Twitchett, 2010). These fluxes may have stimulated marine phytoplankton blooms and intensified oceanic anoxia (Shen et al., 2013b). However, empirical data in support of such a scenario are limited, with no indication of globally elevated marine productivity (Shen et al., 2015) and evidence for a drawdown rather than an increase in oceanic sulfate concentrations (Luo et al., 2010) during the end-Permian crisis and its aftermath.

The most likely alternative is an oceanic mechanism whereby large-scale greenhouse gas emissions linked to flood basalt volcanism (presumably of the Siberian Traps LIP; Reichow et al., 2009) resulted in ocean-surface warming and intensified oceanic stratification (Sun et al., 2012; Song HY et al., 2013) that in turn caused enhanced oceanic anoxia and expansion of intermediate-depth oceanic oxygen-minimum zones (Algeo et al., 2011; Winguth and Winguth, 2012). Large-scale emission of volcanic gasses was suggested by ocean acidification during the earliest Triassic biocrisis (Clarkson et al., 2015). The alternative is environmental changes by the volcanic eruptions in South China area and the convergent continent margins (Yin et al., 1992). Upward expansion of the top of the oxygen-minimum zone, which is equivalent to the "chemocline upward excursion" of Kump et al. (2005), introduced ^{32}S- and ^{12}C-enriched deeper euxinic waters into the ocean-surface layer. This oceanic mechanism is favored because it is consistent with a variety of lines of observational data and theoretical considerations. This mechanism suggests a possible direct link between expansion of oceanic oxygen-minimum zones and the two mass extinction episodes of the Permian–Triassic transition via reductions in habitable ecospace (see Section 5.4), although it is also possible that the correlation of expanded anoxia and mass extinction was a coincidental effect of both being driven by strong climatic warming (Sun et al., 2012).

5.6. Timing and significance of oceanic perturbations relative to the LPME

The timing of oceanic environmental perturbations relative to the LPME is not well established. Many studies have assumed that end-Permian environmental disturbances and the biotic response to them were effectively coeval (e.g., Grice et al., 2005), an assumption that derives from the condensed nature of some PTB sections (e.g., Meishan GSSP) and the low resolution of many chemostratigraphic studies. One point on which consensus exists is that perturbations to the global carbon cycle commenced prior to the LPME, as reflected in the onsets of negative shifts in both carbonate and organic carbon isotopes prior to the mass extinction horizon in many PTB sections (Korte and Kozur, 2010, and references therein). Recent radiometric dating suggests that the onset of the globally recognized $\delta^{13}C_{carb}$ excursion began ~60 kyr prior to the LPME in the Meishan GSSP (Shen SZ et al., 2011; Burgess et al., 2014). The Xiakou section has a $\delta^{13}C_{carb}$ profile similar to that of Meishan, characterized by an initial decrease in the upper *C. changxingensis* Zone and reaching an excursion minimum at the base of the *H. latidentatus-C. meishanensis* Zone (Fig. 3).

Relatively few studies have documented perturbations prior to the mass extinction event in other (i.e., non-C-isotope) oceanic environmental proxies. The Xiakou section shows an abrupt onset of fluctuations in multiple proxies at ~18 cm below the LPME (Fig. 4), recording a major perturbation to the oceanic environment at that time. This 18-cm interval represents ~10 kyr based on a 60-kyr duration for the pre-extinction negative $\delta^{13}C_{carb}$ excursion (Shen SZ et al., 2011; Burgess et al., 2014), which extends over a 1.2-m interval below the LPME at Xiakou (Fig. 3). The implications of these estimates are that the effects of the trigger for the PTB crisis (e.g., the onset of Siberian Traps LIP magmatism) were felt by the global carbon cycle ~50 kyr before oceanic environmental changes became pronounced on the South China Craton, and that these environmental changes in turn preceded the mass extinction event by ~10 kyr. This timeline may be consistent with a gradually accelerating release of thermogenic methane from the Siberian Craton that, following a lag of several tens of thousands of years, resulted in measurable ocean-surface warming and expansion of oceanic anoxic zones.

The apparent delay of the LPME event by ~10 kyr relative to oceanic environmental changes may have several explanations. One possibility is that environmental changes in the 10-kyr interval prior to the LPME were due to a limited forcing (e.g., by intrusive magmatic activity of the Siberian Traps LIP; Reichow et al., 2009), and that the pace of environmental change accelerated abruptly at the LPME (e.g., due to a transition to a major eruptive phase of the Siberian Traps LIP). This hypothesis is consistent with the rapid negative $\delta^{13}C_{carb}$ shift seen globally at the LPME (Korte and Kozur, 2010), if this shift primarily reflects a single mechanism, i.e., thermogenic methane release (Retallack and Jahren, 2008). A second possibility is that gradually deteriorating oceanic environmental conditions (Shen et al., 2012b) finally overstepped a critical threshold at the LPME, triggering a major biocrisis. In this case, the acceleration of the negative $\delta^{13}C_{carb}$ shift cannot be explained only by inputs of ^{13}C-depleted methane (which would have increased slowly in parallel with environmental deterioration) but would require a second source, e.g., ^{13}C-depleted soil carbon liberated through enhanced terrestrial erosion (e.g., Xie et al., 2005, 2007). Either of these possibilities is potentially consistent with chemocline upward excursions (Kump et al., 2005) and an expansion of sulfidic waters into the ocean-surface layer (e.g., Algeo et al., 2008).

6. Conclusions

Integration of high-resolution Fe-speciation, pyrite morphologic, and sulfur isotope data from the Xiakou section, Hubei Province, South China provides significant insights regarding redox conditions and oceanic perturbations during the PTB crisis. Oceanic environmental conditions were relatively stable during the pre-extinction Late Permian but experienced at least two major perturbations with the initial one commencing ~10 kyr prior to the 1st mass extinction horizon (Bed 25 in the Meishan D GSSP). Redox conditions were euxinic during the pre-extinction Late Permian, and subsequently fluctuated between ferruginous and euxinic during and following the extinction interval. The most intense euxinic episodes were associated with the 1st and 2nd extinction horizons, respectively of latest Permian and earliest Triassic age. Ferruginous conditions may have resulted from low concentrations of seawater sulfate and high fluxes of volcanically sourced Fe to the Xiakou environment. The two main intervals of oceanic perturbation and intensified euxinia at Xiakou correlate with the two phases of marine extinction and microbial bloom events (i.e., Beds 25 and 28) in the Meishan GSSP. The observation that these two events are associated with volcanic tuffs at both Xiakou and Meishan suggests that volcanic eruptions or their attendant effects were responsible for the two mass extinction events as well as concurrent oceanic environmental perturbations in the South China region.

Acknowledgements

We thank Drs. Simon Poulton and David Bond for constructive reviews of the manuscript, and Dr. Martin Frank for editorial handling. We are grateful to Prof. H.F. Yin for commenting on this manuscript. Many thanks to Lidan Lei, Zihu Zhang, and Chengsheng Jin for the organic carbon isotope and iron speciation analysis in China University of Geosciences (Wuhan), and Prof. Barry Maynard at the University of Cincinnati for assistance with the extraction of pyrite. This work was supported by National Natural Science Foundation of China (41402001, 41473007, 41572005, 41272024 and 41272372), 111 Project (B08030), the MOST Special Fund from the State Key Laboratory of Geological Processes and Mineral Resources, China University of Geosciences (MSFGPMR10, MSFGPMR02), and the fundamental Research Funds for the Central Universities, China University of Geo-

sciences, Wuhan (CUG160625). Research by TJA is supported by the U.S. National Science Foundation (Sedimentary Geology and Paleobiology program NSF-EAR 1053449), the NASA Exobiology program (NNX13AJ1IG), and the China University of Geosciences, Wuhan (SKL-GPMR program GPMR201301, and SKL-BGEG program BGL21407). This work is a contribution to IGCP Projects 572 and 630.

Appendix A. Supplementary material

Supplementary material related to this article can be found online at http://dx.doi.org/10.1016/j.epsl.2016.03.030.

References

Algeo, T.J., Twitchett, R., 2010. Anomalous Early Triassic sediment fluxes due to elevated weathering rates and their biological consequences. Geology 38, 1023–1026.

Algeo, T.J., Shen, Y.A., Zhang, T.G., Lyons, T.W., Bates, S.M., Rowe, H., Nguyen, T.K.T., 2008. Association of ^{34}S-depleted pyrite layers with negative carbonate δ^{13}C excursions at the Permian/Triassic boundary: evidence for upwelling of sulfidic deep-ocean watermasses. Geochem. Geophys. Geosyst. 9, Q04025.

Algeo, T.J., Kuwahara, K., Sano, H., Bates, S., Lyons, T., Elswick, E., Hinnov, L., Ellwood, B., Moser, J., Maynard, J.B., 2011. Spatial variation in sediment fluxes, redox conditions, and productivity in the Permian–Triassic Panthalassic Ocean. Palaeogeogr. Palaeoclimatol. Palaeoecol. 308, 65–83.

Algeo, T., Henderson, C.M., Ellwood, B., Rowe, H., Elswick, E., Bates, S., Lyons, T., Hower, J.C., Smith, C., Maynard, J.B., Hays, L., Summons, R., Fulton, J., Freeman, K., 2012. Evidence for a diachronous Late Permian marine crisis from the Canadian Arctic region. Geol. Soc. Am. Bull. 124, 1424–1448.

Bond, D.P.G., Wignall, P.B., 2010. Pyrite framboid study of marine Permian–Triassic boundary sections: a complex anoxic event and its relationship to contemporaneous mass extinction. Geol. Soc. Am. Bull. 122, 1265–1279.

Bond, D.P.G., Wignall, P.B., 2014. Large igneous provinces and mass extinctions: an update. In: Keller, G., Kerr, A.C. (Eds.), Volcanism, Impacts, and Mass Extinctions: Causes and Effects. In: Spec. Pap., Geol. Soc. Am., vol. 505, pp. 29–55.

Burgess, S.D., Bowring, S.A., Shen, S.Z., 2014. High-precision timeline for Earth's most severe extinction. Proc. Natl. Acad. Sci. USA 111, 3316–3321.

Canfield, D.E., Raiswell, R., Westrich, J.T., Reaves, C.M., Berner, R.A., 1986. The use of chromium reduction in the analysis of reduced inorganic sulfur in sediments and shales. Chem. Geol. 54, 149–155.

Chen, Z.Q., Benton, M.J., 2012. The timing and pattern of biotic recovery following the end-Permian mass extinction. Nat. Geosci. 5, 375–383.

Clarkson, M.O., Kasemann, S.A., Wood, R.A., Lenton, T.M., Daines, S.J., Richoz, S., Ohnemueller, F., Meixner, A., Poulton, S.W., Tipper, E.T., 2015. Ocean acidification and the Permo-Triassic mass extinction. Science 348, 229–232.

Erwin, D.H., Bowring, S.A., Jin, Y.G., 2002. End-Permian mass-extinctions: a review. In: Koeberl, C., MacLeod, K.G. (Eds.), Catastrophic Events and Mass Extinctions: Impacts and Beyond. In: Spec. Pap., Geol. Soc. Am., vol. 356, pp. 353–383.

Feng, Q.L., He, W.H., Gu, S.Z., Meng, Y.Y., Jin, Y.X., Zhang, F., 2007. Radiolarian evolution during the latest Permian in South China. Glob. Planet. Change 55, 177–192.

Gorjan, P., Kaiho, K., Kakegawa, T., Niitsuma, S., Chen, Z.Q., Kajiwara, Y., Nicora, A., 2007. Paleoredox, biotic and sulfur-isotope changes associated with the end-Permian mass extinction in the western Tethys. Chem. Geol. 244, 483–492.

Grice, K., Cao, C.Q., Love, G.D., Bottcher, M.E., Twitchett, R.J., Grosjean, E., Summons, R.E., Turgeon, S.C., Dunning, W., Jin, Y.X., 2005. Photic zone euxinia during the Permian–Triassic superanoxic event. Science 307, 706–709.

Isozaki, Y., 1997. Permo-Triassic boundary superanoxia and stratified superocean: records from lost deep sea. Science 276, 235–238.

Jin, Y.G., Wang, Y., Wang, W., Shang, Q.H., Cao, C.Q., Erwin, D.H., 2000. Pattern of marine mass extinction near the Permian–Triassic boundary in South China. Science 289, 432–436.

Korte, C., Kozur, H.W., 2010. Carbon-isotope stratigraphy across the Permian–Triassic boundary: a review. J. Asian Earth Sci. 39, 215–235.

Kump, L.R., Pavlov, A., Arthur, M.A., 2005. Massive release of hydrogen sulfide to the surface ocean and atmosphere during intervals of oceanic anoxia. Geology 33, 397–400.

Liu, G.C., Feng, Q.L., Shen, J., Yu, J.X., He, W.H., Algeo, T.J., 2013. Decline of siliceous sponges and spicule miniaturization induced by marine productivity collapse and expanding anoxia during the Permian–Triassic crisis in South China. Palaios 28, 664–679.

Luo, G.M., Kump, L.R., Wang, Y.B., Tong, J.N., Arthur, M.A., Yang, H., Huang, J.H., Yin, H.F., Xie, S.C., 2010. Isotopic evidence for an anomalously low oceanic sulfate concentration following end-Permian mass extinction. Earth Planet. Sci. Lett. 300, 101–111.

Nielsen, J.K., Shen, Y.A., Piasecki, S., Stemmerik, L., 2010. No abrupt change in redox condition caused the end-Permian marine ecosystem collapse in the East Greenland Basin. Earth Planet. Sci. Lett. 291, 32–38.

Poulton, S.W., Canfield, D.E., 2005. Development of a sequential extraction procedure for iron: implications for iron partitioning in continentally derived particulates. Chem. Geol. 214, 209–221.

Poulton, S.W., Canfield, D.E., 2011. Ferruginous conditions: a dominant feature of the ocean through Earth's history. Elements 7, 107–112.

Reichow, M.K., Pringle, M.S., Al'Mukhamedov, A.I., Allen, M.B., Andreichev, V.L., Buslov, M.M., Davies, C.E., Fedoseev, G.S., Fitton, J.G., Inger, S., Medvedev, A.Y., Mitchell, C., Puchkov, V.N., Safonova, I.Y., Scott, R.A., Saunders, A.D., 2009. The timing and extent of the eruption of the Siberian Traps large igneous province: implications for the end-Permian environmental crisis. Earth Planet. Sci. Lett. 277, 9–20.

Retallack, G.J., Jahren, A.H., 2008. Methane release from igneous intrusion of coal during Late Permian extinction events. J. Geol. 116, 1–20.

Riccardi, A.L., Arthur, M.A., Kump, L.R., 2006. Sulfur isotope evidence for chemocline upward excursions during the end-Permian mass extinction. Geochim. Cosmochim. Acta 70, 5740–5752.

Shen, J., Algeo, T.J., Hu, Q., Zhang, N., Zhou, L., Xia, W., Xie, S., Feng, Q., 2012a. Negative C-isotope excursions at the Permian–Triassic boundary linked to volcanism. Geology 40, 963–966.

Shen, J., Algeo, T.J., Zhou, L., Feng, Q.L., Yu, J.X., Ellwood, B.B., 2012b. Volcanic perturbations of the marine environment in South China preceding the latest Permian extinction event and their biotic effects. Geobiology 10, 82–103.

Shen, J., Algeo, T.J., Feng, Q.L., Zhou, L., Feng, L.P., Zhang, N., Huang, J.H., 2013a. Volcanically induced environmental change at the Permian–Triassic boundary (Xiakou, Hubei Province, South China): related to West Siberian coal-field methane releases? J. Asian Earth Sci. 75, 95–109.

Shen, J., Lei, Y., Algeo, T.J., Feng, Q.L., Servais, T., Yu, J.X., Zhou, L., 2013b. Volcanic effects on microplankton during the Permian–Triassic transition (Shangsi and Xinmin, South China). Palaios 28, 552–567.

Shen, J., Schoepfer, S.D., Feng, Q.L., Zhou, L., Yu, J.X., Song, H.Y., Wei, H.Y., Algeo, T.J., 2015. Marine productivity changes during the end-Permian crisis and Early Triassic recovery. Earth-Sci. Rev. 149, 136–162.

Shen, S.Z., Crowley, J.L., Wang, Y., Bowring, S.A., Erwin, D.H., Sadler, P.M., Cao, C.Q., Rothman, D.H., Henderson, C.M., Ramezani, J., Zhang, H., Shen, Y., Wang, X.D., Wang, W., Mu, L., Li, W.Z., Tang, Y.G., Liu, X.L., Liu, L.J., Zeng, Y., Jiang, Y.F., Jin, Y.G., 2011. Calibrating the end-Permian mass extinction. Science 334, 1367–1372.

Shen, Y.A., Farquhar, J., Zhang, H., Masterson, A., Zhang, T.G., Wing, B.A., 2011. Multiple S-isotope evidence for episodic shoaling of anoxic water during Later Permian mass extinction. Nat. Commun. 2, 210. http://dx.doi.org/10.1038/ncomms1217.

Song, H.J., Wignall, P.B., Tong, J.N., Yin, H.F., 2013. Two pulses of extinction during the Permian–Triassic crisis. Nat. Geosci. 6, 52–56.

Song, H.Y., Tong, J.N., Algeo, T.J., Horacek, M., Qiu, H.H.J., Tian, L., Chen, Z.Q., 2013. Large vertical gradients in Early Triassic seas of the South China implications for oceanographic changes related to Traps volcanism. Glob. Planet. Change 105, 7–20.

Song, H.Y., Tong, J., Algeo, T.J., Song, H.J., Qiu, H.O., Zhu, Y., Tian, L., Bates, S., Lyons, T.W., Luo, G.M., Kump, L.R., 2014. Early Triassic seawater sulfate drawdown. Geochim. Cosmochim. Acta 128, 98–113.

Sun, Y.D., Joachimski, M.M., Wignall, P.B., Yan, C.B., Chen, Y.L., Jiang, H.S., Wang, L.N., Lai, X.L., 2012. Lethally hot temperatures during the early Triassic greenhouse. Science 388, 366–370.

Svensen, H., Planke, S., Polozov, A.G., Schmidbauer, N., Corfu, F., Podladchikov, Y.Y., Jamtveit, B., 2009. Siberian gas venting and the end-Permian environmental crisis. Earth Planet. Sci. Lett. 277, 490–500.

Wang, G.Q., Xia, W.C., 2004. Conodont zonation across the Permian–Triassic boundary at the Xiakou section, Yichang city, Hubei Province, and its correlation with the global stratotype section and point of the PTB. Can. J. Earth Sci. 41, 323–330.

Wignall, P.B., Twitchett, R.J., 1996. Oceanic anoxia and the end-Permian mass extinction. Science 272, 1155–1158.

Wilkin, R.T., Barnes, H., Brantley, S., 1996. The size distribution of framboidal pyrite in modern sediments: an indicator of redox conditions. Geochim. Cosmochim. Acta 60, 3897–3912.

Winguth, C., Winguth, A.M.E., 2012. Simulating Permian–Triassic oceanic anoxia distribution: implications for species extinction and recovery. Geology 40, 127–130.

Xiang, L., Schoepfer, S.D., Zhang, H., Yuan, D.X., Cao, C.Q., Zheng, Q.F., Henderson, C.M., Shen, S.Z., 2016. Oceanic redox evolution across the end-Permian mass extinction at Shangsi, South China. Palaeogeogr. Palaeoclimatol. Palaeoecol. 448, 59–71.

Xie, S.C., Pancost, R.D., Yin, H.F., Wang, H.M., Evershed, R.P., 2005. Two episodes of microbial change coupled with Permo/Triassic faunal mass extinction. Nature 434, 494–497.

Xie, S.C., Pancost, R.D., Huang, J.H., Wignall, P.B., Yu, J.X., Tang, X.Y., Chen, L., Huang, X.Y., Lai, X.L., 2007. Changes in the global carbon cycle occurred as two episodes during the Permian–Triassic crisis. Geology 35, 1083–1086.

Yin, H.F., Huang, S.J., Zhang, K.X., Hansen, H.J., Yang, F.Q., Ding, M.H., Bie, X.M., 1992. The effects of volcanism on the Permo-Triassic mass extinction in South China. In: Sweet, W.C., Yang, Z., Dickins, J.M., Yin, H. (Eds.), Permo-Triassic Events in the Eastern Tethys. Cambridge University Press, Cambridge, pp. 169–174.

Yin, H.F., Zhang, K.X., Tong, J.N., Yang, Z.Y., Wu, S.B., 2001. The Global Stratotype Section and Point (GSSP) of the Permian–Triassic boundary. Episodes 24, 102–114.
Yin, H.F., Xie, S.C., Luo, G.M., Algeo, T.J., Zhang, K.X., 2012. Two episodes of environmental change at the Permian–Triassic boundary of the GSSP section Meishan. Earth-Sci. Rev. 115, 163–172.
Yin, H.F., Jiang, H.S., Xia, W.C., Feng, Q.L., Zhang, N., Shen, J., 2014. The end-Permian regression in South China and its implication on mass extinction. Earth-Sci. Rev. 137, 19–33.
Zhao, L.S., Chen, Y.L., Chen, Z.Q., Cao, L., 2013. Uppermost Permian to lower Triassic conodont zonation from Three Gorges area, South China. Palaios 28, 523–540.